

Insights into hyperbolic phonon polaritons in hBN using Raman scattering from encapsulated transition metal dichalcogenide layers

Jacob J.S. Viner ¹, Liam P. McDonnell ¹, Pasqual Rivera ², Xiaodong. Xu ², David C. Smith ^{1*}

¹ School of Physics and Astronomy, University of Southampton, Southampton SO17 1BJ, United Kingdom.

² Department of Physics, University of Washington, Seattle, WA, USA

Abstract

New techniques for probing hyperbolic phonon polaritons (HPP) in 2D materials will support the development of the emerging technologies in this field. Previous reports have shown that it is possible for WSe₂ monolayers in contact with the hexagonal boron nitride (hBN) to generate HPP in the hBN via Raman scattering. In this paper, we set out new results on HPP Raman scattering induced in hBN by WSe₂ and MoSe₂ monolayers including new resonances at which the Raman scattering is enhanced. Analysis of the observed Raman lineshapes demonstrates that Raman scattering allows HPP with wavevectors with magnitudes significantly in excess of 15000 cm⁻¹ to be probed. We present evidence that the Raman scattering can probe HPP with frequencies less than the expected lower bound on the Reststrahlen band suggesting new HPP physics still waits to be discovered.

Intro

The unique properties of hyperbolic phonon polaritons (HPPs)^{1–4} are leading to their exploitation in a range of important applications^{5,6}. For instance, in the production of a new class of mid-infrared sources⁷ which, whilst thermally excited, produce radiation which is narrowband⁸ and spatially coherent^{9,10}. Work on related sources indicates that it should be possible to combine these properties with high modulation frequencies; up to 10 MHz¹¹. Another field in which HPPs are being exploited is MIR integrated nanophotonics for applications in surface-enhanced infrared spectroscopy¹² as well as sub-diffraction imaging^{6,13}. A recent highlight in this field has been the creation of reconfigurable waveguides and lenses for hyperbolic phonon polaritons^{14,15} using phase change materials. Hyperbolic phonon polaritons allow subwavelength volume confinement^{6,16,17} of mid-infrared radiation by as much as a factor of 86. This confinement is not only being exploited for miniaturisation but also allows the concentration of electromagnetic energy, allowing for strong coupling^{18,19} and nonlinear effects^{20–22}. By analogy with plasmonics, which are more lossy than HPP²³, an even wider range of HPP applications, e.g. biosensors²⁴ and improving signal to noise photodetectors^{7,8}, are likely to emerge soon.

The two main techniques used to study HPP are FTIR spectroscopy²⁵ and scattering-type scanning near-field optical microscopy (s-SNOM)^{26–28}. FTIR is simpler however it either requires specially prepared microfabricated structures⁵ or prism coupling^{5,29} to access the large wavevector HPP. The former is not suitable for probing HPP in devices and the latter limits the wavevector that can be accessed. s-SNOM^{26–28} allows HPPs to be imaged in real space with impressive resolution and thus access to wavevectors of the order of ~ 1000 times the free space wavevector^{27,28}. However, this technique is complex and requires physical contact with the sample.

A HPP measurement method based upon the conversion of MIR to visible radiation would enable a wide range of new opportunities. The relative maturity of visible photonics means that such a

method is likely to be much simpler. It should allow high-resolution (0.5 μm) imaging without the need for a near-field probe and because many of the key HPP are wide band gap materials it should allow imaging of sub-surface HPP. Due to the much shorter wavelength of visible light such a method might allow access to even larger wavevector HPPs. Actually, it has already been shown that transition metal dichalcogenide (TMD) layers allow the probing of HPPs via Raman scattering of visible radiation^{30–32}. However, no one has explored what information about HPP can be obtained from the Raman spectra. In this paper we present significant new results on HPP Raman scattering in TMDs. These include new resonances at which the HPP Raman features are enhanced in WSe₂ monolayers and the first measurements of HPP Raman features in Mo based TMDs. Based upon these new results we discuss the mechanism for HPP Raman scattering; the fact that it can access much higher wavevector HPP than IR based techniques; and what Raman scattering of HPP might bring to the field of HPP technologies.

Main Body

Figure 1a) shows a Raman spectrum of the encapsulated WSe₂ monolayer taken with an excitation energy of 1.866 eV. The observed Raman features can be separated into single- and multi-phonon peaks in the spectral range up to around 750 cm^{-1} and two features at around 730-850 cm^{-1} and 1000-1080 cm^{-1} . These have previously been associated with scattering of excitons in the monolayer by hBN HPP (lower shift feature) and a combination of a hBN HPP and a monolayer A_{1'} phonon (upper shift feature). The peaks at smaller Raman shifts, which only involve phonons, are characteristically narrower with widths of the order of 0.25 meV (2 cm^{-1}) whereas the HPP related features are significantly broader, at 10 meV (80 cm^{-1}). This can also be observed in Figure 1b) and c) where we present colourmaps of the resonance Raman spectra of an encapsulated WSe₂ monolayer. All of the features show clear resonance behaviour in the colourmaps. For instance the Raman peak at 250 cm^{-1} , assigned to the degenerate A_{1'}/E' phonons^{33,34}, has four resonances; when the incoming and scattered photons are resonant with the A1s and A2s bright excitonic states. As previously reported, the 730-850 cm^{-1} features shows a clear outgoing resonance with the A1s state and incoming resonance with the A2s state^{31,32}. As also previously reported, the 1000-1080 cm^{-1} shows a strong resonance at \sim 1.865 eV which is both an outgoing resonance with the A1s and an incoming resonance with the A2s, i.e. a double resonance. In addition, the same features have at least two other resonances at higher laser energies which have not been reported before. The clearest of these is an outgoing resonance associated with the A2s exciton. There is also a weaker resonance, approximately 20 meV higher in energy corresponding to the A3s exciton. As more clearly shown in Figure 1b), the features at the outgoing resonances show a characteristic behaviour in which the higher shift scattering is resonant at higher laser energies. This is particularly visible from 1.95 to 2 eV. This is clear proof that the two broad features, with Raman shifts centred at approximately 800 and 1050 cm^{-1} , can be associated with a band of excitations rather than a single underlying excitation.

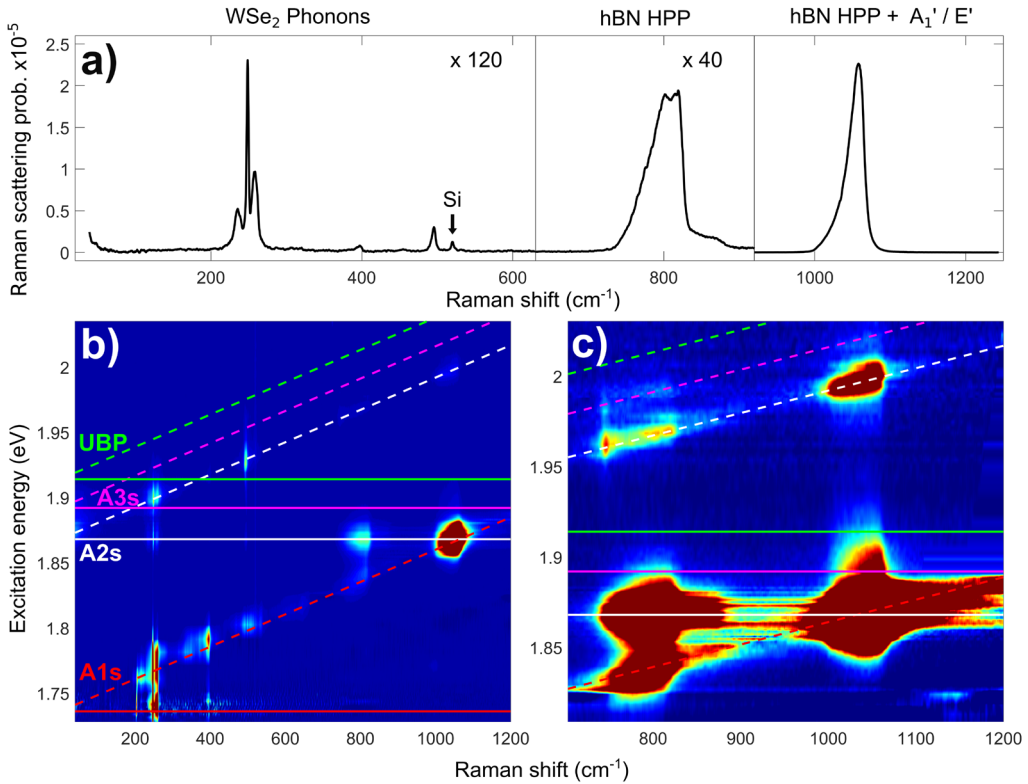


Figure 1: a) An individual Raman spectrum from the hBN encapsulated WSe₂ sample with an excitation energy of 1.866 eV. The first two parts of the spectrum are scaled by a factor of 120 and 40 for visibility. b) and c) show colourmaps of the resonance behaviour of the 800 and 1050 cm⁻¹ hBN Raman features b) presents the full spectral width including lower Raman shift features from the WSe₂ phonons, such as the strong 250 cm⁻¹ A_{1'}(Γ)/E'(Γ) peak, as well as the higher shift hBN modes. c) Presents a zoom of the higher shift part of the spectra presented in b) with the colours adjusted to show a narrower range of intensities. The colour indicates the intensity of the Raman scattering in logarithmic scale, with blue corresponding to lowest and red to highest intensity. The energies of the incoming and outgoing Raman resonances (solid and dashed lines) associated with the A_{1s}, A_{2s} and A_{3s} excitonic states are shown with red, white and pink lines respectively. The green lines correspond to the resonance conditions for the lowest energy unbound electron hole pair (UBP). The signal around 1.87 eV between the 800 and 1050 cm⁻¹ peaks and shifts above 1100 cm⁻¹ are from photoluminescence from the A_{1s} exciton, which follows the A_{1s} outgoing resonance.

In order to better understand the resonance behaviour and to determine the energy of the excitonic states involved, resonance profiles of the Raman scattering were determined for the two features as presented in Figure 2. As each feature is associated with a band of excitations, the extracted resonance profile changes at different Raman shifts across the feature. For both of these hBN features, 3 resonance profiles were determined; each by integrating the Raman scattering for a 5 cm⁻¹ band around a centre Raman shift. This process is described in the supplementary section S2. The resonance profiles presented in Figure 2 clearly show the A_{1s} outgoing and A_{2s} incoming resonances previously observed³⁰⁻³², as well as the new higher energy resonances. Interestingly there is no statistically significant Raman scattering associated with the hBN related features at the A_{1s} incoming resonance. However, the significant additional noise due to the strong A_{1s} luminescence means the upper limit on any scattering at these laser energies is comparable with the strength of the Raman scattering at the highest energy resonances. In the case of the 730-850 cm⁻¹ feature, shown in Figure 2a), the A_{1s} outgoing resonance near 1.83 eV shifts to lower energy, as expected, for the lower centre Raman shifts. The two higher energy resonances above 1.95 eV show the same behaviour indicating they are also both outgoing resonances. For the 1000-1080 cm⁻¹ feature profiles shown in Figure 2b), the A_{1s} outgoing and A_{2s} incoming resonances fall at the same energy, creating a double resonance with the measured Raman scattering two orders of magnitude greater than that of the Raman feature at 730-850 cm⁻¹.

The resonance profiles were all fitted using the standard third-order perturbation theory prediction for Raman scattering [SI] that assumes that the exciton-phonon scattering occurs in a single step. In order to fit all of the resonance requires a minimum of three excitonic states. Unfortunately, this requires six exciton-phonon scattering matrix elements. This makes getting a unique fit for these parameters impossible. However, the energy and lifetime parameters for the three excitons obtained from the six independent resonance profiles, with and without setting some of the scattering matrix elements to zero, were remarkably consistent as shown in supplementary section S2. These fits give the energy (with fit estimated errors) for the three excitonic states to be 1.735 ± 0.002 , 1.867 ± 0.001 & 1.892 ± 0.005 . The first two energies are to within experimental error the same as the A1s and A2s energies obtained from fits to reflectivity spectra³⁵ and separate fits to the A_{1'} phonon's resonance profiles. The third energy is in agreement to within a few meV with previously published values for the A3s excitonic state^{36,37}. This is the first time that a Raman resonance with the A3s state has been reported.

Based upon the agreement between the measured energies of the first three excitonic energies and our model for the Rydberg series³⁸ we can predict the energy of the remaining excitonic states and the minimum energy unbound electron-hole states. As shown with green lines in Figure 1, the threshold for excitation of unbound electron-hole states is less than the laser energy associated with the A2s and A3s outgoing resonances. Thus, it is possible that the initial optically excited state at these resonances is a real, unbound pair excitation rather than a virtual excitonic state.

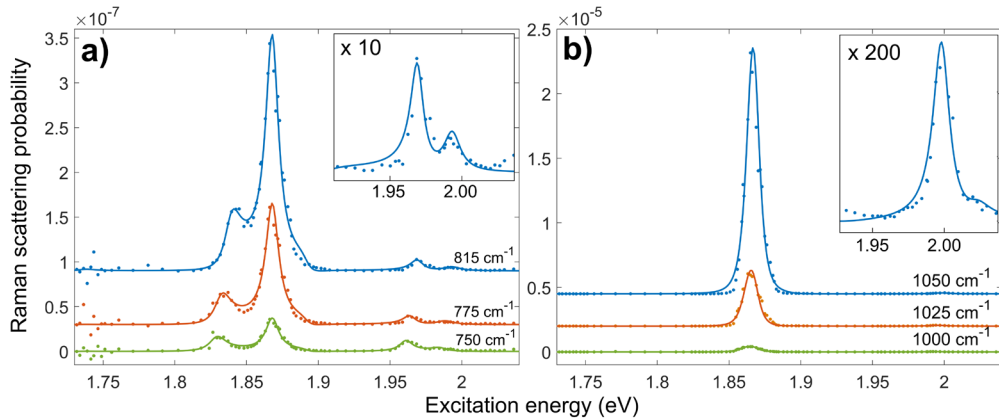


Figure 2: Resonance profiles for the a) 800 cm^{-1} or b) 1050 cm^{-1} hBN Raman features determined at different Raman shifts within the feature. The insets present vertically scaled subsections of the 815 and 1050 cm^{-1} resonance profiles. Peaks in the resonance profile observed in this range are associated with the A2s and A3s outgoing resonance conditions. The solid lines show fits to the resonance behaviour using 3-state, third-order, perturbation-theory resonant Raman scattering models where the three states are the A1s, A2s & A3s excitons in WSe₂. The resonances at ~ 1.84 eV and between 1.95 and 2.0 eV are outgoing resonances and thus change energy with Raman shift. The resonance at ~ 1.85 eV is the A2s incoming resonance. The A1s incoming resonance would fall around 1.74 eV but no statistically significant Raman signal is observed. The noise in the resonance data at the energy of the A1s exciton is photoluminescence signal from the A1s exciton and trion.

One of the key characteristic features of the hBN related Raman scattering are their broad lineshapes. However, as shown in Figure 3, the observed lineshape depends on the resonance and the energy of the laser relative to the peak of the resonance. This is more obvious at the outgoing resonance but also true at the incoming resonances. The qualitative differences between the resonances can be rationalised as being due to the variation of the resonance conditions across the lineshape and how these depend on laser energy. For instance, the relative suppression of the

higher Raman shift scattering at an outgoing resonance for lower laser energies is because the lower shift scattering is closer to resonance with the outgoing state. However attempts to quantitatively correct for this effect to obtain a single underlying lineshape did not produce a consistent lineshape independent of the laser energy. Despite this, it is possible to draw some general conclusions about the underlying lineshape. In particular, for the $730\text{-}850\text{ cm}^{-1}$ feature the lineshape covers the whole of the Reststrahlen band. In fact, at the low shift side of peak the lineshape continues smoothly beyond the Reststrahlen band. In general, the highest scattering is closer to the upper bound of the Reststrahlen band however the exact form of the peak varies with the resonance. The lineshape of the $1000\text{-}1080\text{ cm}^{-1}$ feature is very similar to the $730\text{-}850\text{ cm}^{-1}$ feature. In this case spanning, and at lower shifts extending beyond, the Reststrahlen band shifted up by 250 cm^{-1} as would be expected if this feature is a due to an emission of a combination of the HPP responsible for the $730\text{-}850\text{ cm}^{-1}$ feature and the A_1'/E' phonon.

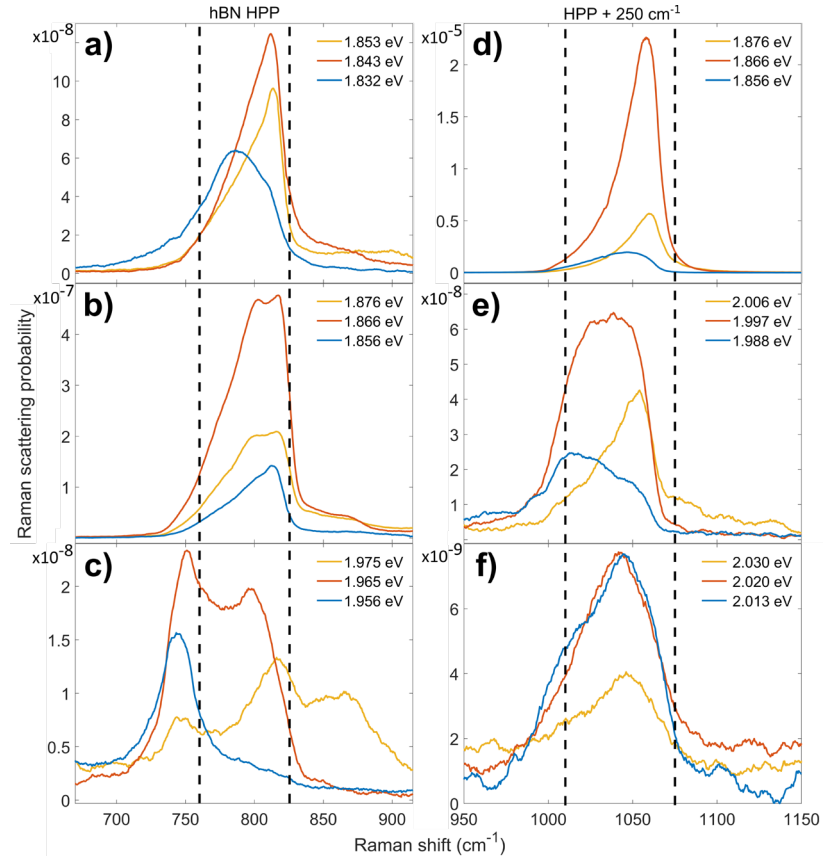


Figure 3: Raman spectra showing the lineshapes of the 800 [a, b, c] and 1050 cm^{-1} [d, e, f] hBN associated Raman peaks at various resonances. The orange curve shows the spectrum at the peak of the specified resonance and the blue and yellow curves show spectra taken at ± 10 meV either side of the resonance. a) A1s outgoing b) A2s incoming c) A2s outgoing d) A1s outgoing = A2s incoming e) A2s outgoing f) A3s outgoing. The lower shift peak observed in c), in the 1.956 eV spectra, at about 750 cm^{-1} is associated with a multi-phonon peak rather than hBN HPP as can be seen more clearly in Fig 1c. This is only observed at the A2s outgoing resonance. The agreement of the shift of this peak with three times the shift of the A_1' peak suggests that it is due to emission of 3 A_1' phonons.

Having fully analysed the data for the encapsulated WSe₂ we now turn our attention to the results for encapsulated MoSe₂. The strength of the hBN related Raman peaks in encapsulated MoSe₂ is

significantly weaker; Fig 4. In MoSe_2 , the features are observed only when the laser energy is tuned to the A2s or B2s excitons. In both cases, the resonances are near double resonances with the A1s and B1s excitons respectively - close to the outgoing photon energy. Due to the weak scattering, it was not possible to obtain clear spectra apart from at the peak of the resonance or fully analyse the resonance behaviour. However, there is considerable new information available from the resonant spectra. In particular, the upper shift feature in MoSe_2 is considerably broader than the lower shift feature. As shown on Fig 4, it is possible to explain this if the upper shift feature is in fact due to a combination of a HPP and either an A_1' or E' phonon. In the case of the WSe_2 these phonons are degenerate and so it is possible that the upper shift feature also involves a contribution from the E' phonon. In addition and importantly, the lineshape of the lower shift feature is very similar to the same feature in WSe_2 and in particular extends beyond the Reststrahlen band at lower shifts. Thus, the observation of Raman scattering outside of the Reststrahlen band is not a feature of a single material or sample but is more general.

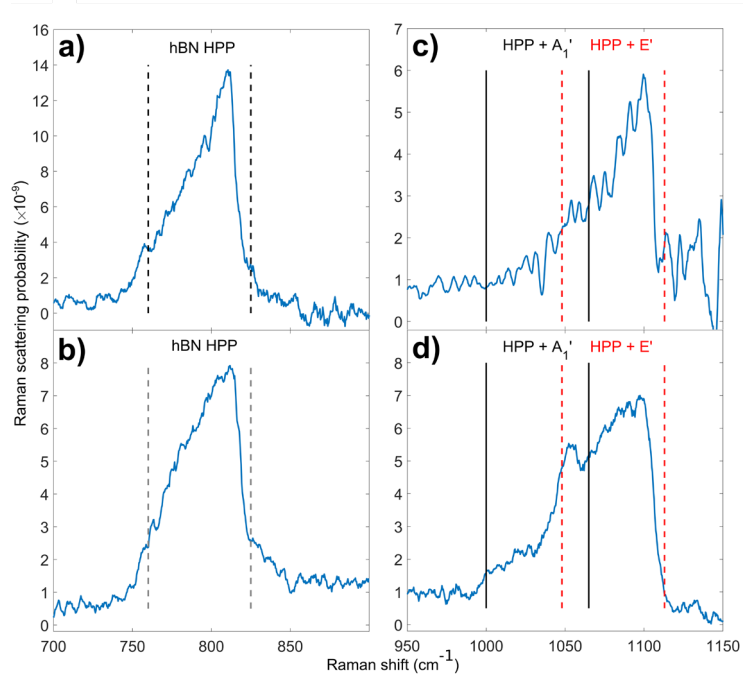


Figure 4: Raman spectra of the hBN encapsulated MoSe_2 monolayer sample. Panels a) & b) show the broad 800 cm^{-1} hBN Raman peak with Reststrahlen band shifts marked with dashed lines. Panels c) & d) show the spectra around 1050 cm^{-1} , with markings at the Reststrahlen band shifts plus the $\text{MoSe}_2 A_1'(\Gamma)$ phonon (240 cm^{-1}) in black and plus the $\text{MoSe}_2 E'(\Gamma)$ phonon (288 cm^{-1}) in red. Panels a) & c) are from spectra taken around the A1s outgoing / A2s incoming resonances at 1.80 eV . Panels b) & d) are from spectra taken with the laser energy between the B1s outgoing resonance and the B2s incoming resonance at 2.01 eV .

Whilst the attribution of the hBN features to HPP is not new, so far no one has tried to understand the lineshape in terms of this model. In order to fully model the Raman lineshape would require a model not only for the HPPs but also a model for TMD excitons and for the HPP-exciton interaction. However, it is reasonable to expect that the density of states of the HPP may well dominate the lineshape. Therefore we have adapted a T-matrix model of the absorption spectrum of HPP developed by Passler et al.³⁹ to predict the HPP dispersion relations. We use the hBN dielectric function determined by Caldwell et al.¹⁶ and layer thicknesses constrained by atomic force

microscopy and fitting to the optical reflectivity spectra. From the IR reflectivity spectra obtained from this model we can extract the centre energy and width of the HPP modes as a function of in-plane wavevector (Fig 5). In an actual reflectivity measurement only very small wavevector HPP, k less than approximately 1100 cm^{-1} , would be accessible. In a Raman experiment the fact that we are probing the states with optical frequency radiation means that we should be able to probe significantly larger wavevectors. If we use the wavelength of light resonant with the A2s exciton in WSe₂ and based upon back scattering of radiation incident at 30° , reasonable for our objective lens, we predict that the maximum wavevector HPP we should generate in momentum conserving Raman scattering would be 15050 cm^{-1} . As shown on Fig 4 this should limit the HPP Raman feature to the range $800\text{--}820\text{ cm}^{-1}$ which is clearly too small a range to explain the observed feature. Defects and other effects can lead to non-momentum conserving Raman scattering. As shown on Fig 4, if we assume the maximum wavevector of HPP observed in Raman scattering is five times that of the maximum momentum conserving wavevector the range of the HPP Raman feature would be predicted to increase significantly to $760\text{--}820\text{ cm}^{-1}$. However even this range is too narrow compared with the observed feature. Fundamentally, it is not possible for the current model to produce scattering below the lower Reststrahlen band edge. Thus, whilst it is highly likely that HPP are responsible for the two features associated with them in Raman spectra of hBN encapsulated TMDs layers the simple HPP model set out above cannot explain the width of these features.

We now need to consider why the simple HPP model fails and what additional physics is required to explain the observed Raman features. An obvious possibility is that we have used the incorrect parameters for the Reststrahlen band. However a review of the literature gives four independent measurements of these parameters based on IR spectroscopy^{16,40–42} and whilst there are variations in the extracted parameters none of the measurements support the lower bound of the Reststrahlen band being below 760 cm^{-1} . Another alternative is that the $730\text{--}850\text{ cm}^{-1}$ is a combination peak involving absorption of a thermal phonon. However, the measurements were performed at 4 K and the thermal energy, which corresponds to $\sim 3\text{ cm}^{-1}$, is insufficient to significantly extend the feature to lower shifts. Another possibility is that at very large wavevectors the ZO phonon responsible for the HPP disperses to lower energy. However, there is no obvious mechanism allowing us to couple to such large wavevector HPP. Thus, currently we do not have a good explanation of the width of the two Raman features associated with HPP in these structures. Whilst it is possible, the resolution of this issue is associated with the TMD layers it is also possible that the ability of Raman scattering to access large wavevector HPP is allowing us to access new HPP effects not yet understood.

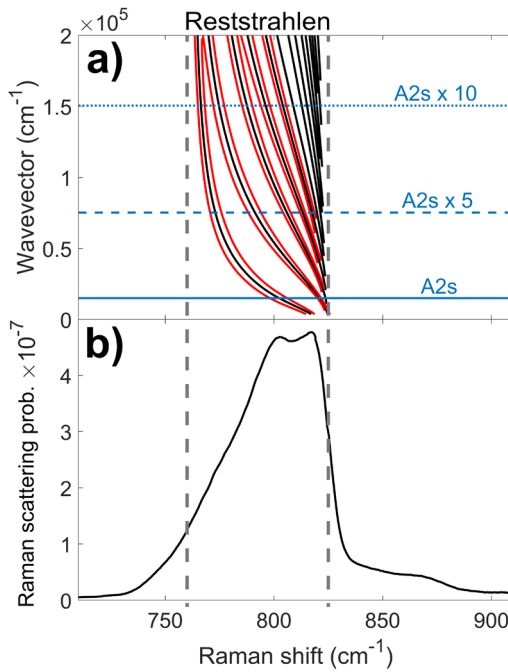


Figure 5: a) Dispersion relation for the hyperbolic phonon polariton modes, determined using the 4x4 transfer matrix approach of Passler et. al.³⁹ The black lines show the bands of allowed modes and the red lines indicate their widths (at half magnitude) for the first five allowed HPP modes. The blue lines indicate the maximum momentum allowed in a single phonon Raman process with the exciting photon resonant at the A2s exciton energy and at 5 and 10 times that momentum. b) shows a Raman spectrum taken on the hBN encapsulated WSe₂ monolayer sample with an excitation energy of 1.866 eV, on resonance with the WSe₂ A2s exciton. The hBN TO and LO frequencies of 760 and 825 cm^{-1} are marked with dashed vertical lines, between which is the Reststrahlen band.

The results set out in this paper add considerably to our knowledge about the hBN HPP Raman features observed previously in hBN encapsulated WSe₂ structures. In WSe₂, we have observed outgoing resonances with the A2s and A3s excitonic states for the first time. The outgoing resonance with the A3s exciton is the first time this exciton has been detected in resonance Raman. In MoSe₂, we have observed hBN HPP features for the first time. In this material, they are associated with double resonances with the incoming photons resonant with the A2s or B2s excitons and the outgoing photons resonant with the A1s or B1s excitons respectively. From the MoSe₂ spectra, we can deduce that in this material the upper HPP feature involves emission of a HPP and either an A_{1'} or E' phonon, with both cases contributing to the overall lineshape. It is quite likely that this is also true for WSe₂ but the degeneracy of the phonons in this material makes this difficult to confirm.

However, the most important outcomes of this study are associated with the HPP. Firstly, it is clear that compared to IR reflectivity measurements, resonance Raman scattering allows access to a much greater range of HPP with larger wavevectors. Even momentum conserving Raman allows access to wavevectors a factor of ten greater than accessible by IR measurements and there is good evidence that Raman scattering is not momentum conserving allowing even larger wavevector modes to be studied. In addition, there is a mystery as to how Raman scattering can occur at Raman shifts below the lower bound on the Reststrahlen band determined from IR measurements. The solution to this mystery may give us insights into HPP that cannot be achieved via other techniques. The insights need not be restricted to HPP associated with the layers of hBN. It is possible to transfer exfoliated TMD flakes onto a wide range of substrates. This suggests they could make an ideal probe for HPP associated with a wide range of materials and metamaterials. This paper shows that doing this will give an insight into HPP in these structures that is difficult to achieve in other ways.

Methods

The hBN encapsulated monolayer MoSe₂ and WSe₂ samples were fabricated by hot pickup using a dry polycarbonate on PDMS stamp from individual mechanically exfoliated monolayers⁴³. The WSe₂ sample was encased within a top 36 nm, and bottom 27 nm, thick hBN layer. The bottom hBN layer was on top of a 20 nm graphite layer which sat atop a 300 nm thick SiO₂ coated Si wafer. The MoSe₂ sample followed the same structure, with top and bottom hBN thicknesses of 30 and 20 nm respectively and a 4nm graphite thickness. These are the same samples that feature in a larger resonance Raman study^{35,44,45} with the same experimental setup. The measurements presented here were performed with the sample under vacuum at 4 K in a helium flow cryostat. A Coherent Mira 900 Ti:Sapphire laser in CW mode and a Coherent CR-599 CW dye laser were used to excite the samples in backscattering geometry via a 50x 0.5 NA long working distance microscope objective. This allowed Raman spectra to be taken with excitation energies from 1.60 to 2.24 eV. The incident power on the sample was 100 μ W. The Raman spectra were measured with a TriVista 555 spectrometer with the first two stages of the spectrometer set in subtractive mode and a liquid nitrogen cooled CCD.

Linear polarisers were placed in the exciting laser beam before the sample and in between the sample and spectrometer. For each excitation energy, Raman spectra were taken with these polarisers set co-linear and with them crossed. The crossed polariser spectra were subtracted from the co-linear spectra which had the effect of removing the photoluminescence (PL) signal whilst preserving the Raman signal. At energies where PL signal in the spectrum was many orders of magnitude greater than the Raman, such as near the A1s exciton energy, residual PL was present after subtraction.

The Raman signal from the SiO₂ coated Si substrate was used to calibrate the Raman spectra for frequency. The intensity of the Si peak was used with Si resonance Raman data from literature⁴⁶ to convert the data to absolute scattering probability. A transfer matrix model of the stack of layers in the samples was used to correct for the effect of thin film interference on the Raman intensity. The details of these corrections are given in the supplementary information of our previous paper³⁵.

Supplementary Information

The supplementary information contains discussion of the hBN modes in a hBN encapsulated MoSe₂ monolayer sample, including a resonance Raman colourmap and resonance profile of the 800 cm^{-1} mode. Additional detail on the extraction and fitting of resonance profiles from the Raman spectra is also provided.

Data Availability

The data presented in this paper is openly available from the University of Southampton Repository DOI: <https://doi.org/10.5258/SOTON/D1734>

Corresponding Author

*D.C.Smith@soton.ac.uk

Author Contributions

Samples were fabricated by P.R. The experimental measurements were performed by J.V and L.P.M. Experimental data analysis and interpretation was carried out by J.V., L.P.M and D.C.S. The paper was written by D.C.S and J.V. All authors discussed the results and commented on the manuscript.

The manuscript was written through contributions of all authors. All authors have given approval to the final version of the manuscript.

Funding Sources

Research at the University of Southampton was supported by the Engineering and Physical Science Council of the UK via programme grant EP/N035437/1. Both L.P.M and J.V were also supported by EPSRC DTP funding. The work at University of Washington was mainly supported by the Department of Energy, Basic Energy Sciences, Materials Sciences and Engineering Division (DE-SC0018171).

Bibliography

1. Jacob, Z. Nanophotonics: Hyperbolic phonon-polaritons. *Nat. Mater.* **13**, 1081–1083 (2014).
2. Yoxall, E. *et al.* Direct observation of ultraslow hyperbolic polariton propagation with negative phase velocity. *Nat. Photonics* **9**, 674–678 (2015).
3. Low, T. *et al.* Polaritons in layered two-dimensional materials. *Nat. Mater.* **16**, 182–194 (2017).
4. Basov, D. N., Fogler, M. M. & García De Abajo, F. J. Polaritons in van der Waals materials. *Science* **354**, (2016).
5. Folland, T. G., Nordin, L., Wasserman, D. & Caldwell, J. D. Probing polaritons in the mid- to far-infrared. *J. Appl. Phys.* **125**, (2019).
6. Li, P. *et al.* Hyperbolic phonon-polaritons in boron nitride for near-field optical imaging and focusing. *Nat. Commun.* **6**, 1–9 (2015).
7. Jones, A. C. & Raschke, M. B. Thermal infrared near-field spectroscopy. *Nano Lett.* **12**, 1475–1481 (2012).
8. Lu, G. *et al.* Narrowband Polaritonic Thermal Emitters Driven by Waste Heat. *ACS Omega* **5**, 10900–10908 (2020).
9. Carminati, R. & Greffet, J. J. Near-field effects in spatial coherence of thermal sources. *Phys. Rev. Lett.* **82**, 1660–1663 (1999).
10. Greffet, J. J. *et al.* Coherent emission of light by thermal sources. *Nature* **416**, 61–64 (2002).

11. Wojszvzyk, L. *et al.* Fast modulation and polarization control of infrared emission by incandescent metasurfaces. in *Plasmonics: Design, Materials, Fabrication, Characterization, and Applications XVIII* (eds. Tanaka, T. & Tsai, D. P.) 20 (SPIE, 2020). doi:10.1117/12.2567481
12. Autore, M. *et al.* Boron nitride nanoresonators for Phonon-Enhanced molecular vibrational spectroscopy at the strong coupling limit. *Light Sci. Appl.* **7**, 17172–17178 (2018).
13. Dai, S. *et al.* Subdiffractive focusing and guiding of polaritonic rays in a natural hyperbolic material. *Nat. Commun.* **6**, 1–7 (2015).
14. Chaudhary, K. *et al.* Polariton nanophotonics using phase-change materials. *Nat. Commun.* **10**, 1–6 (2019).
15. Folland, T. G. *et al.* Reconfigurable infrared hyperbolic metasurfaces using phase change materials. *Nat. Commun.* **9**, 1–7 (2018).
16. Caldwell, J. D. *et al.* Sub-diffractive volume-confined polaritons in the natural hyperbolic material hexagonal boron nitride. *Nat. Commun.* **5**, 1–9 (2014).
17. Lee, I. H. *et al.* Image polaritons in boron nitride for extreme polariton confinement with low losses. *Nat. Commun.* **11**, (2020).
18. Gubbin, C. R. *et al.* Hybrid longitudinal-transverse phonon polaritons. *Nat. Commun.* **10**, 1–6 (2019).
19. Passler, N. C. *et al.* Strong Coupling of Epsilon-Near-Zero Phonon Polaritons in Polar Dielectric Heterostructures. *Nano Lett.* **18**, 4285–4292 (2018).
20. Paarmann, A. *et al.* Second harmonic generation spectroscopy in the Reststrahl band of SiC using an infrared free-electron laser. *Appl. Phys. Lett.* **107**, (2015).
21. Razdolski, I. *et al.* Resonant Enhancement of Second-Harmonic Generation in the Mid-Infrared Using Localized Surface Phonon Polaritons in Subdiffractive Nanostructures. *Nano Lett.* **16**, 6954–6959 (2016).
22. Passler, N. C. *et al.* Second-Harmonic Generation from Critically Coupled Surface Phonon Polaritons. *ACS Photonics* **4**, 1048–1053 (2017).
23. Caldwell, J. D. *et al.* Low-loss, extreme subdiffraction photon confinement via silicon carbide localized surface phonon polariton resonators. *Nano Lett.* **13**, 3690–3697 (2013).
24. Rodrigo, D. *et al.* Mid-infrared plasmonic biosensing with graphene. *Science* **349**, 165–168 (2015).
25. Giles, A. J. *et al.* Ultralow-loss polaritons in isotopically pure boron nitride. *Nat. Mater.* **17**, 134–139 (2018).
26. Dai, S. *et al.* Tunable phonon polaritons in atomically thin van der Waals crystals of boron nitride. *Science* **343**, 1125–1129 (2014).
27. Fei, Z. *et al.* Gate-tuning of graphene plasmons revealed by infrared nano-imaging. *Nature* **486**, 82–85 (2012).
28. Chen, J. *et al.* Optical nano-imaging of gate-tunable graphene plasmons. *Nature* **487**, 77–81 (2012).
29. Folland, T. G. *et al.* Probing hyperbolic polaritons using infrared attenuated total reflectance micro-spectroscopy. *MRS Commun.* **8**, 1418–1425 (2018).

30. Du, L. *et al.* Strong and tunable interlayer coupling of infrared-active phonons to excitons in van der Waals heterostructures. *Phys. Rev. B* **99**, 1–9 (2019).
31. Chow, C. M. *et al.* Unusual Exciton-Phonon Interactions at van der Waals Engineered Interfaces. *Nano Lett.* **17**, 1194–1199 (2017).
32. Chen, B. *et al.* Interlayer electron–phonon coupling in WSe₂/hBN heterostructures. *Nat. Phys.* **13**, 127–131 (2016).
33. Zhao, W. *et al.* Lattice dynamics in mono- and few-layer sheets of WS₂ and WSe₂. *Nanoscale* **5**, 9677 (2013).
34. Chen, S. Y., Zheng, C., Fuhrer, M. S. & Yan, J. Helicity-Resolved Raman Scattering of MoS₂, MoSe₂, WS₂, and WSe₂ Atomic Layers. *Nano Lett.* **15**, 2526–2532 (2015).
35. McDonnell, L. P., Viner, J., Rivera, P., Xu, X. & Smith, D. C. Observation of Intravalley Phonon Scattering of 2s Excitons in MoSe₂ and WSe₂ Monolayers. *2D Mater.* (2020).
36. Manca, M. *et al.* Enabling valley selective exciton scattering in monolayer WSe₂ through upconversion. *Nat. Commun.* **8**, 1–7 (2017).
37. Chen, S. Y. *et al.* Luminescent Emission of Excited Rydberg Excitons from Monolayer WSe₂. *Nano Lett.* **19**, 2464–2471 (2019).
38. Viner, J. J. S. *et al.* Excited Rydberg States in TMD Heterostructures. *arXiv* (2021). doi:2103.09004
39. Passler, N. C. & Paarmann, A. Generalized 4×4 matrix formalism for light propagation in anisotropic stratified media: study of surface phonon polaritons in polar dielectric heterostructures. *J. Opt. Soc. Am. B* **34**, 2128 (2017).
40. Geick, R., Perry, C. H. & Rupprecht, G. Normal modes in hexagonal boron nitride. *Phys. Rev.* **146**, 543–547 (1966).
41. Ordin, S. V., Sharupin, B. N. & Fedorov, M. I. Normal lattice vibrations and the crystal structure of anisotropic modifications of boron nitride. *Semiconductors* **32**, 924–932 (1998).
42. Franke, E. *et al.* Phase and microstructure investigations of boron nitride thin films by spectroscopic ellipsometry in the visible and infrared spectral range. *J. Appl. Phys.* **82**, 2906–2911 (1997).
43. Zomer, P. J., Guimarães, M. H. D., Brant, J. C., Tombros, N. & Van Wees, B. J. Fast pick up technique for high quality heterostructures of bilayer graphene and hexagonal boron nitride. *Appl. Phys. Lett.* **105**, (2014).
44. McDonnell, L. P. *et al.* Superposition of intra- and inter-layer excitons in twistronic MoSe₂/WSe₂ bilayers probed by resonant Raman scattering. *2D Mater.* **8**, 35009 (2021).
45. McDonnell, L. P. *et al.* Experimental realisation of Dual Periodicity Moiré Superlattice in a MoSe₂/WSe₂ Heterobilayer. *arXiv* (2020). doi:2009.07676
46. Aggarwal, R. L. *et al.* Measurement of the absolute Raman cross section of the optical phonon in silicon. *Solid State Commun.* **151**, 553–556 (2011).

**Supplementary information for Insights into hyperbolic phonon polaritons in
hBN using Raman scattering from encapsulated transition metal
dichalcogenide layers**

Jacob J.S. Viner ¹, Liam P. McDonnell ¹, Pasqual Rivera ², Xiaodong. Xu ², David C. Smith ^{1*}

¹ School of Physics and Astronomy, University of Southampton, Southampton SO17 1BJ, United Kingdom.

² Department of Physics, University of Washington, Seattle, WA, USA

Table of Contents

S1) Details Resonance Model Fitting Procedure	2
S2) Monolayer MoSe₂ Resonance Raman	4

S1) Details Resonance Model Fitting Procedure

The resonance profiles of these broad hBN peaks were obtained by averaging the intensity over a range of 5 cm^{-1} centred at a chosen Raman shift for each Raman spectrum. It is this averaged Raman scattering probability, $I(E)$, as a function of excitation energy, that was fitted to the 3 state third order perturbation theory model for absolute scattering probability:

$$I(E) = \left| \sum_{i,j=1}^3 \frac{a_{ij}}{(E - E_i - i\Gamma_i)(E - E_j - E_{p1} - i\Gamma_j)} \right|^2 \quad (1)$$

Where E_i is the energy of the state i , and Γ_i is the width; E_{p1} is the phonon energy; a_{ij} represents the matrix element for the scattering channel involving states i and j ; and E is the excitation energy. This amplitude a_{ij} is complex, and during the fitting process it is treated as a real amplitude multiplied by $e^{i\theta}$ where θ is between 0 and 2π . The resonance profiles at the chosen centre Raman shifts of 750, 775, 815, 1000, 1025 and 1050 cm^{-1} , represented in Figure S1 by the coloured bands, were fitted separately.

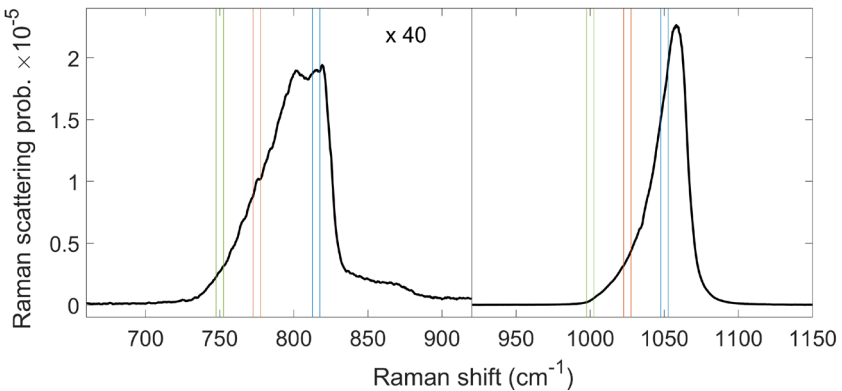


Figure S1: Subsection of the Raman spectrum presented in Fig 1 of the main body of the paper. The spectrum was taken with an excitation energy of 1.866 eV on the hBN encapsulated monolayer WSe₂ sample. The data below 930 cm^{-1} was scaled by a factor of 40 for comparison. The bands of energies averaged over to extract the resonance profiles presented in the paper are marked with pairs of coloured lines.

The best-fit parameters for the six WSe₂ resonance profiles presented in Fig 2 in the main body of the paper are presented in Table S1. Here, the real part of the scattering matrix element squared corresponds to the Raman scattering probability. The energies of the three excitons from the fits to all six resonance profiles all agree to within 6 meV. The widths are generally in good agreement; to within two standard errors of each other. Additional details on the derivation of the resonance model are given in the supplementary information of our previous work^{S1}.

		Raman shift (cm ⁻¹)					
	Scattering Channel	750	775	815	1000	1025	1050
Absolute Raman scattering probability (x10 ⁻¹⁶)	A1s - A1s	2.29±0.95	7.4±1.2	32±3	189.5±8.4	60.6±43	81±2400
	A1s - A2s	9.55±0.02	40.5±0.12	70.0±0.14	17.65±0.16	56.2±0.3	986±13
	A1s - A3s	3.10±0.36	50.4±0.67	69±1	7.3±1.1	300±17	100±960
	A2s - A2s	0.062±3.9	0.13±23	97±2.7	409±83	350±780	1000±66000
	A2s - A3s	16.6±1.3	13±19	19.1±2.0	71.6±45	1820±370	0±22000
	A3s - A3s	6.1±2.7	15±34	99±7.1	756±21	560±250	1300±3400
Energy (eV)	A1s	1.736±0.001	1.736±0.005	1.738±0.001	1.734±0.001	1.732±0.001	1.736±0.001
	A2s	1.868±0.0004	1.867±0.0004	1.867±0.0002	1.869±0.001	1.869±0.001	1.865±0.003
	A3s	1.891±0.003	1.890±0.007	1.892±0.001	1.895±0.017	1.894±0.003	1.897±0.005
Width (meV)	A1s	6.0±1.1	6.4±0.4	6.5±0.8	8.7±1.1	5.9±0.3	7.9±1.1
	A2s	6.0±0.5	5.6±0.3	5.3±0.2	7.0±0.7	6.9±0.4	7.0±0.1
	A3s	10.0±7.0	10.8±1.1	10.5±1.4	8±14	4.8±2.0	4.2±2.0

Table S1: Fitting parameters from the resonance Raman profiles taken at different Raman shifts across the 800 and 1050 cm⁻¹ broad hBN Raman features in the hBN encapsulated monolayer WSe₂ sample. The corresponding profiles are shown in Figure 2 in the main body of the paper. The errors given are standard deviations determined from the fitting process.

S2) Monolayer MoSe₂ Resonance Raman

Figure S2 shows a colourmap of resonance Raman data on an encapsulated MoSe₂ monolayer. In this case, the scattering from the TMD associated Raman peaks, which fall below 650 cm⁻¹, was generally more intense than that from the hBN modes. The TMD Raman peaks show resonant enhancement at the A1s, A2s, B1s and B2s excitons as described in our previous work^{S1}, with the 2s states appearing weaker due to their lower oscillator strength. In Figure S2a) the incoming and outgoing resonances associated with each exciton are indicated by the solid and dashed lines respectively with the colour of the lines indicated if the state is an A (white) or B (red) excitonic state. The incoming resonances at the energies of the excitons are marked with solid lines and the outgoing resonances, at the exciton energy plus the phonon energy, are indicated with dashed lines. The Si Raman peak from the sample substrate is present at 520 cm⁻¹ across the entire range of excitation energies used.

Scattering from the broad 800 and 1050 cm⁻¹ hBN modes is observed around 1.8 eV, falling between the A1s outgoing and A2s incoming resonances which are indicated by white lines. Example Raman spectra showing the lineshape of the modes at 1.8 eV are given in Figure S2c) & e). Strong PL signal which follows the A1s outgoing resonance appears with the feature at 1050 cm⁻¹ between the A1s outgoing and A2s incoming resonance energies. Scatter from these hBN modes is also visible around 2.0 eV which falls between the B1s outgoing and B2s incoming resonances, indicated in Red. The lineshapes at this energy are shown in Figure S2b) & d). Notably, no clear resonance is observed in the colourmap between the B1s incoming resonance and the A2s outgoing resonance. Unlike the WSe₂ case (see Fig 3 in main paper) in the monolayer MoSe₂ spectra we do not observe any features near 750 cm⁻¹ which could be associated with multi-phonon TMD Raman modes. In MoSe₂ we also note the intensity of the hBN peaks is strongest at double resonances associated with a 1s outgoing and 2s incoming resonance, with minimal scattering observed between A and B excitons. It is also interesting to note that the 1050 cm⁻¹ feature is less intense than the one at 800 cm⁻¹, unlike the WSe₂ case. This is despite being much closer to a double resonance condition than the 800 cm⁻¹ feature.

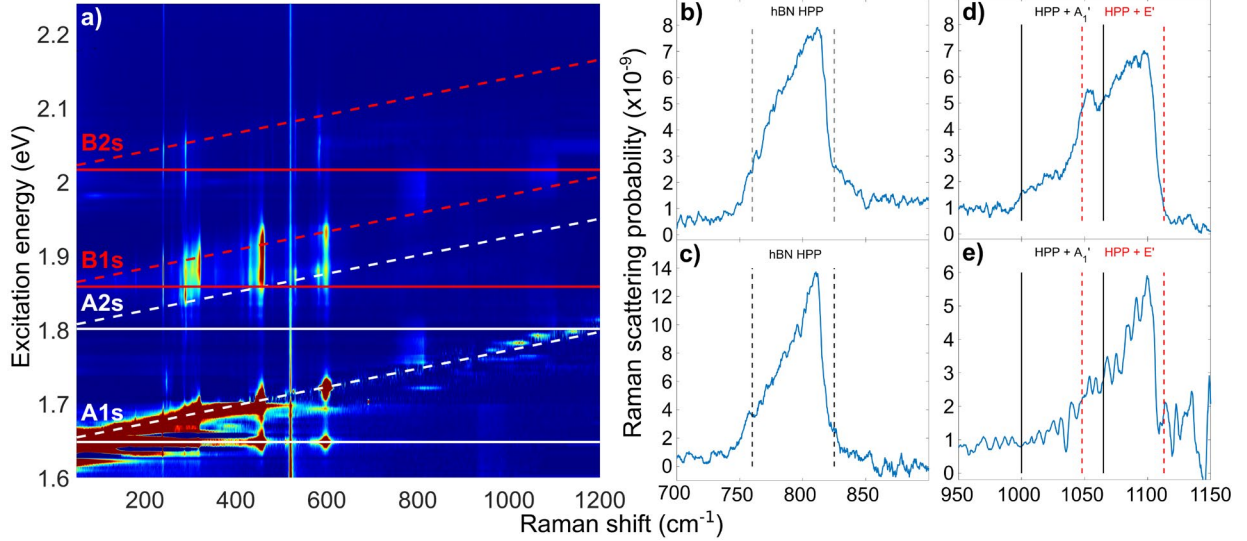


Figure S2: a) Colourmap of a resonance Raman spectra taken at 4 K of monolayer MoSe₂ encapsulated in hBN with excitation energies from 1.6 to 2.25 eV. The resonance energies associated with the A1s and A2s excitons are shown in white and the B1s and B2s shown in red, with solid lines corresponding to the incoming resonance and the dashed lines corresponding to the outgoing resonances at the exciton energy plus the phonon energy. The intensity of the Raman scattering is indicated in logarithmic scale by the colour, with dark red corresponding to most intense and dark blue least intense. b)-e) subsections of Raman spectra of MoSe₂ reproduced from the main body of the paper showing the lineshape of the two hBN HPP associated modes. The upper two plots correspond to an excitation energy of 2.01 eV and the lower two plots are 1.80 eV.

In Figure S2 a resonance Raman profile for the 800 cm⁻¹ hBN peak in MoSe₂ is shown. This profile was extracted, by averaging the intensity of the Raman signal for shifts between 797.5 and 802.5 cm⁻¹, for each of the spectra. The strongest signal is present between the 1s outgoing and 2s incoming resonances. This is true for both the A and B excitons and suggests strong inter-state scattering for A1s-A2s and B1s-B2s. The signal at the 1s incoming and 2s outgoing energies is not as intense, suggesting that the amplitudes of the scattering involving a single excitonic state are small.

The data was fitted to a four-state resonance model. The best fit obtained is shown on the figure. The four-state model takes the same form as the three-state model used for WSe₂, given in equation (1), with the sum taken up to 4 rather than 3. This model requires 10 scattering terms, one for scattering via each of the 4 excitons individually, and 6 corresponding to inter-state scattering.

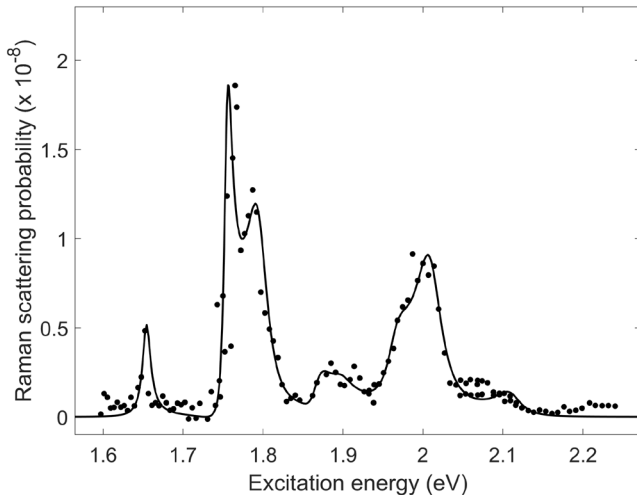


Figure S3: Resonance Raman profile extracted for the MoSe_2 hBN 800 cm^{-1} peak shown in Figure S2 with a four-state resonance Raman scattering model fitted to the data. The excitation energies used range from $1.60 - 2.24 \text{ eV}$, spanning from below the MoSe_2 $\text{A}1s$ exciton to above the $\text{B}2s$ exciton.

Whilst the fitted profile shows reasonable qualitative agreement with the resonance data the uncertainties associated with the fitted amplitudes are orders of magnitude larger than the obtained amplitude coefficients. This arises due to overfitting of the resonance data, where the large number of amplitude terms required in the four-state model can take multiple possible values, preventing the fit from converging towards a single solution. This is partly a consequence of the fact that the amplitude terms can combine in both addition and subtraction, depending on their phase, leading to multiple possible solutions. The parameter correlation matrix for the fitted model is illustrated in Figure S4 as a colour-map. The top left hand 10×10 square of high intensity corresponds to the correlation between the amplitude terms in the fit. The 10×9 area at the top right corresponds to the correlation between the amplitude and phase terms and the 9×9 area in the bottom right corner is the correlation between the phase terms. The remaining area corresponds to correlation with the fitted energy and width terms with themselves and all other parameters. The ‘blue cross’ indicates that there are no strong correlations between the energies and widths and all the other parameters. Thus, the uncertainties in amplitude and phase do not affect the ability of the fit to constrain the energies and widths. This is also reflected in the confidence intervals for these parameters that are of the order of 10 meV.

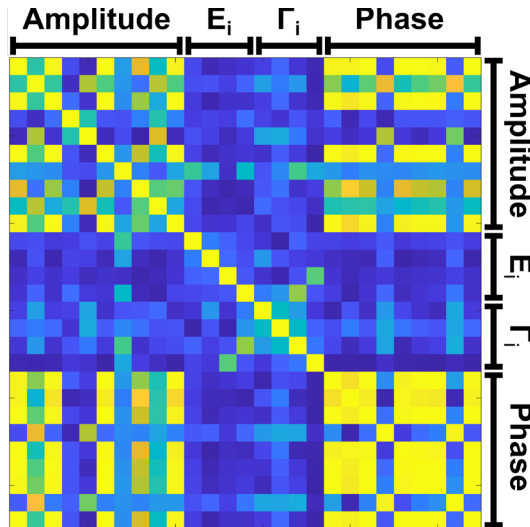


Figure S4: Visualisation of the magnitude of the parameter correlation matrix for the fitting parameters in the 4-state resonance fit. Blue is close to zero (no correlation) and yellow is close to 1 (maximum correlation). The first 10 terms are the amplitudes, the next four are the energies of the excitonic states followed by the four widths. The final 9 are the phases of the scattering channels, where the A2s-A2s channel is set to zero phase.

These fitted energies of the excitonic states all agree to within 6 meV of the values determined from fitting resonance Raman profiles of the $240\text{ cm}^{-1} A_1'(\Gamma)$ MoSe₂ phonon. For this phonon, the resonance data was fitted to a single state resonance model at the A1s, a two-state model at the A2s and B1s and another single state model at the B2s^{S1}. The energies and widths are given for both of these cases in Table S2. The widths are generally broader for the hBN HPP fit however, the much larger uncertainties mean that it is not significant.

Exciton	MoSe ₂ fitted exciton energy (eV)		MoSe ₂ fitted exciton width (meV)	
	A ₁ '(Γ) phonon profiles	hBN HPP profile	A ₁ '(Γ) phonon profiles	hBN HPP profile
A1s	1.648 ± 0.001	1.654 ± 0.003	3.0 ± 0.1	6.2 ± 3.3
A2s	1.804 ± 0.001	1.796 ± 0.013	8.2 ± 1.7	17.0 ± 7.5
B1s	1.858 ± 0.001	1.860 ± 0.020	18.9 ± 1.3	17.1 ± 15.2
B2s	2.016 ± 0.001	2.012 ± 0.010	9.4 ± 0.7	21.5 ± 14.0

Table S2: Energy and width coefficients of the A1s, A2s, B1s and B2s excitons from fitting the broad 800 cm^{-1} hBN mode resonance Raman profile for the hBN encapsulated MoSe₂ monolayer. These are given alongside equivalent energies and widths determined by fitting the resonance Raman profiles of the $240\text{ cm}^{-1} A_1'(\Gamma)$ MoSe₂ phonon from the same Raman spectra. The errors given are standard deviations determined from the fitting process.

References

S1. McDonnell, L. P., Viner, J., Rivera, P., Xu, X. & Smith, D. C. Observation of Intravalley Phonon Scattering of 2s Excitons in MoSe₂ and WSe₂ Monolayers. *2D Mater.* (2020).